Massachusetts Institute of Technology

Gravity Currents in Aquatic Canopies

Y. Tanino

Department of Civil and Environmental Engineering, Massachusetts Institute of Technology, Cambridge, Massachusetts, USA

H. M. Nepf

Department of Civil and Environmental Engineering, Massachusetts Institute of Technology, Cambridge, Massachusetts, USA

P. S. Kulis

Department of Civil Engineering, University of Texas at Austin, Austin, Texas, USA

Abstract. A lock exchange experiment is used to investigate the propagation of gravity currents through a random array of rigid, emergent cylinders which represents a canopy of aquatic plants. As canopy drag increases, the propagating front varies from the classic profile of an unobstructed gravity current to a triangular profile. Unlike the unobstructed lock exchange, the gravity current in the canopy decelerates with time as the front lengthens. Two drag-dominated regimes associated with linear and non-linear drag laws are identified. The theoretical expression for toe velocity is supported by observed values. Empirical criteria are developed to predict the current regime from the cylinder Reynolds number and the array density.

1. Introduction

Gravity-driven convective currents in the sidearms and littoral zones of reservoirs have been studied in the field [e.g., *Adams and Wells*, 1984], in the laboratory [e.g., *Lei and Patterson*, 2002; *Sturman and Ivey*, 1998], and through modelling [e.g., *Brocard and Harleman*, 1980; *Farrow and Patterson*, 1993; *Horsch et al.*, 1994]. These flows are driven by spatial heterogeneity in the temperature, and thus density, that may result from spatial variability in water depth [e.g., *Monismith et al.*, 1990; *Roget and Colomer*, 1996], groundwater discharge [*Roget et al.*, 1993], light compensation depth [e.g., *MacIntyre et al.*, 2002; *Nepf and Oldham*, 1997], shading due to floating macrophytes [*Coates and Ferris*, 1994], or sheltering from the wind [*MacIntyre et al.*, 2002]. Aquatic gravity currents also occur in estuaries where salt water and freshwater meet [*O'Donnell*, 1993]. *Simpson* [1997] presents additional examples and a comprehensive review of gravity currents.

In shallow systems, aquatic vegetation will often be present and can influence the propagation of a gravity current by providing a mechanism for energy dissipation. For example, *Oldham and Sturman* [2001] have demonstrated that steady, buoyancy-driven, down-slope flow decreases with decreasing permeability within a vegetated region. However, estimated timescales of circulation formation [*Wells and Sherman*, 2001] and response to forcing [*Farrow and Patterson*, 1993] strongly suggest that diurnally-forced convective currents are often unsteady under typical field conditions [e.g., *Farrow and Patterson*, 1993; *Wells and Sherman*, 2001]. Here, we examine the behavior of unsteady front propagation.

Lock-exchange flows have been studied extensively through both laboratory experiments and numerical

modelling. These flows can easily be produced in a laboratory tank by installing a removable partition. The resulting two reservoirs are filled with fluids of different density. When the partition is removed, the horizontal density gradient generates an exchange flow. The heavier fluid propagates towards the lighter fluid reservoir along the bottom of the tank and the lighter fluid propagates along the free surface in the opposite direction [*Simpson*, 1997].

The classic lock exchange has negligible dissipation and is inertia-dominated. It exhibits a predominantly horizontal interface that curves sharply toward the free surface and the bed at the leading edges of the surface current and undercurrent, respectively [*Benjamin*, 1968]. In contrast, exchange flows through sand are drag-dominated, and the interface is inclined to the horizontal plane, rotating about its mid-point [*Keulegan*, 1954]. Figure 1 illustrates these two limits.

This paper examines the behavior of exchange flows between the two limits, specifically obstructed lock exchange under drag conditions representative of aquatic canopies. The goal of this paper is to document and explain the transition from the inertia-dominated regime to the drag-dominated regime. Our mathematical description of front propagation is validated with our experimental observation. The transition between regimes is classified by the cylinder Reynolds number and the dimensionless array drag.

2. Mathematical Formulation

The two-dimensional Cartesian coordinate system (x, z) is defined with $x = 0$ at the lock and $z = 0$ at the bed (Figure 2). The x-axis is aligned with the direction of the undercurrent. Emergent vegetation is modelled by an array of randomly distributed cylinders of diameter d that span the water column. The cylinder array contains N elements distributed over the horizontal footprint of the tank, A. The porosity, $n = 1 - (\pi/4)\,ad$, defines the volume fraction of fluid within the array, where $a = Nd/A$ is the frontal area of the cylinders per unit volume. The components of the pore velocity of the fluid (u, w) are aligned with the axes (x, z), respectively. When the lock is removed, the fluid of higher density (ρ_1) flows in the $+\hat{x}$ direction and the fluid of lower density (ρ_2) flows in the $-\hat{x}$ direction, forming two layers separated by the interface $\eta(x, t)$, as shown in Figure 2. From scale analysis it can be shown that viscous stresses in the fluid are small compared to the array drag in the current experiment (Section 4). Similarly, turbulent stresses are negligible if $ad > 0.005$ [*Burke and Stolzenbach*, 1983], which is satisfied in all but three of the obstructed experimental runs (Table 1).

Accounting for the volume fraction occupied by the cylinders and assuming a quadratic drag law, we obtain the two-dimensional momentum equation for a cylinder array

$$n\frac{Du}{Dt} = -n\frac{1}{\rho}\frac{\partial P}{\partial x} - \frac{C_D a u|u|}{2}, \qquad (1)$$

where C_D is the array drag coefficient, ρ is the fluid density, and P is the hydrostatic pressure. Equation 1 is strictly valid only at spatial scales that encompass multiple cylinders, by definition of C_D. Note that despite the anisotropy of the cylinder array, the average planar porosity is equivalent to the volumetric porosity [*Brenner and Edwards*, 1993, p. 188].

If the drag term is negligible, Equation 1 reduces to

the classic unobstructed lock exchange, for which the interface $\eta(x,t)$ is predominantly horizontal. The leading edges, or toes, of this current propagate at the steady velocity [e.g., *Shin et al.*, 2004]

$$u_{toe} = \pm\sqrt{g'\frac{H}{4}} = \pm\sqrt{\frac{g\Delta\rho}{\rho}\frac{H}{4}}. \qquad (2)$$

Here, g' is the reduced gravity based on $\Delta\rho$, the density difference between the two layers, $g = 980$ cm s^{-2} is the gravitational acceleration, and H is the total water depth [*Shin et al.*, 2004]. In this scenario u_{toe} is independent of time because of the absence of energy sources and sinks.

In this study, we are interested in defining u_{toe} when the drag dominates inertia. Scaling the inertial term as $u\partial u/\partial x \sim u_{toe}^2/L$, we expect from Equation 1 that array drag dominates inertia when $C_D aL/n \geq O(10)$. Under these conditions, Equation 1 reduces to a balance between only array drag and buoyancy:

$$u|u|(x,t) = -\frac{2n}{C_D a}\frac{1}{\rho}\frac{\partial P}{\partial x}. \qquad (3)$$

The hydrostatic pressure, P, in the lower ($z \leq \eta(x,t)$) and upper ($\eta(x,t) < z \leq H$) layers is described respectively as

$$P_1(x,z,t) = P_0(x,t) - \rho_1 gz \qquad (4)$$

and

$$P_2(x,z,t) = P_0(x,t) - \rho_1 g\eta(x,t) - \rho_2 g(z - \eta), \qquad (5)$$

where $P_0(x,t)$, $P_1(x,z,t)$, and $P_2(x,z,t)$ are the pressure at the bed ($z = 0$), in the lower layer, and the upper layer, respectively. Because $\partial P/\partial x$ is independent of z within each layer, u as defined in Equation 3 for each layer is also independent of z.

In a lock exchange, temporal and spatial variations in H are insignificant, and therefore neglected. Then, mass conservation requires zero net flux at each vertical cross-section and

$$nu_1\eta = -nu_2(H - \eta), \qquad (6)$$

where u_1 and u_2 are velocities in the lower and upper layer, respectively.

The application of Equations 3, 4, and 5 to Equation 6 yields an expression for the pressure gradient along the bed,

$$\frac{1}{\rho_1}\frac{\partial P_0(x,t)}{\partial x} = g'\frac{\partial \eta}{\partial x}\frac{\left(1 - \frac{\eta}{H}\right)^2}{\left(1 - \frac{\eta}{H}\right)^2 + \left(\frac{\eta}{H}\right)^2}, \qquad (7)$$

where $g' = g(\rho_1 - \rho_2)/\rho_1$. For simplicity, we have used the approximation $\rho_1 = \rho_2$, valid for our experiments ($\rho_1/\rho_2 \leq 1.05$) and for most field conditions. Then, the flow velocity in the lower and upper layers, respectively, is

$$u_1^2(x,t) = -\frac{2n}{C_D a}g'\frac{\partial \eta}{\partial x}\frac{\left(1 - \frac{\eta}{H}\right)^2}{\left(1 - \frac{\eta}{H}\right)^2 + \left(\frac{\eta}{H}\right)^2} \qquad (8)$$

and

$$u_2|u_2|(x,t) = \frac{2n}{C_D a}g'\frac{\partial \eta}{\partial x}\frac{\left(\frac{\eta}{H}\right)^2}{\left(1 - \frac{\eta}{H}\right)^2 + \left(\frac{\eta}{H}\right)^2}. \qquad (9)$$

Evaluating Equations 8 and 9 at the toes ($\eta = 0$ and $\eta = H$, respectively) yields

$$u_{toe}(t) = \sqrt{-\frac{2n}{C_D a} g' \frac{\partial \eta}{\partial x}\Big|_{\eta=0}} \qquad (10)$$

in the lower layer and

$$u_{toe}(t) = -\sqrt{-\frac{2n}{C_D a} g' \frac{\partial \eta}{\partial x}\Big|_{\eta=H}} \qquad (11)$$

in the upper layer. An analytical expression for $\partial \eta(x,t)/\partial x$ could not be found. However, if the interface is self-similar, its gradient can be described as

$$\frac{\partial \eta}{\partial x}(x,t) = -S\frac{H}{L}, \qquad (12)$$

where $L(t)$ is the longitudinal frontal length (Figure 2) and $S(x/L)$ is the scale constant. Observations of the interface gradient at $x = 0$, discussed later, support the assumption of self-similar behavior. Then, Equations 10 and 11 simplify to

$$u_{toe}(t) = \sqrt{\frac{2n}{C_D a L} g' H S_{\eta=0}} \qquad (13)$$

and

$$u_{toe}(t) = -\sqrt{\frac{2n}{C_D a L} g' H S_{\eta=H}}, \qquad (14)$$

respectively.

An estimate of the array drag coefficient C_D is necessary to evaluate Equations 13 and 14. C_D may be a function of the cylinder Reynolds number $Re = |u| d / \nu$ and the dimensionless array density, ad. For a smooth, isolated circular cylinder in the Re range $1 < Re < 10^5$, C_D is described by the empirical expression [*White*, 1991, p. 183]

$$C_D \approx 1 + 10.0 Re^{-\frac{2}{3}}. \qquad (15)$$

Unfortunately, a comprehensive description of cylinder drag in an array has not yet been developed. Previous studies suggest that C_D in an array is suppressed for $Re \geq O(100)$ due to sheltering [e.g., *Raupach*, 1992]. However, Equation 15 remains reasonable for $ad < 0.03$ [*Nepf*, 1999]. In contrast, C_D is enhanced in low Re ranges [*Koch and Ladd*, 1997]. For example, numerical simulations show that C_D in a random array of 5% solid volume fraction (equivalent to $a = 0.1$ cm^{-1} for cylinders used in the present study) and $Re < 35$ behaves as [*Koch and Ladd*, 1997, Figure 26]

$$C_D \approx \frac{2}{Re}(12 + 1.07 Re), \qquad (16)$$

which predicts a higher C_D than Equation 15 for $Re < 35$. This dependence on Re and array density allows the solution to Equations 8 and 9 to take on many forms and prevents the derivation of a general analytical solution.

Under low $Re (< 1)$ C_D may approach a linear drag law regime, as implied by Equation 16, where C_D is inversely proportional to Re. Under this condition, an analytic expression for $\eta(x,t)$ derived by *Huppert and Woods* [1995] is applicable. Using $C_D = C'/|u|$, where C' is a constant,

Equation 3 becomes

$$u(x,t) = -\frac{2n}{C'a}\frac{1}{\rho}\frac{\partial P}{\partial x}, \qquad (17)$$

which is the expression used by *Huppert and Woods* [1995], with $2n/(C'a\rho)$ replacing their ratio of permeability over dynamic viscosity k/μ. Following their analysis, one can arrive at the similarity solution for interface position,

$$\frac{\eta(x,t)}{H} = \frac{1}{2}\left(1 - \frac{x}{\sqrt{\beta t}}\right), \qquad (18)$$

where $\beta \equiv 2ng'H/(C'a)$. The sign change from the original solution reflects the reversal in the direction of propagation of the undercurrent from the formulation of *Huppert and Woods* [1995]. This solution describes a linear interface that passes through $(x,z) = (0, H/2)$ with the leading edges $(x_{toe} = \pm\sqrt{\beta t})$ propagating at velocity

$$u_{toe} = \frac{dx_{toe}}{dt} = \pm\frac{1}{2}\sqrt{\frac{\beta}{t}} = \pm\frac{\beta}{L}, \qquad (19)$$

where $L = 2|x_{toe}|$.

In summary, theory predicts that array drag will manifest itself in two ways. First, unlike the classic lock exchange, gravity currents propagating through an array decelerate as the front lengthens (Equations 13, 14, and 19). Second, the interface deviates from the classic profile described by *Benjamin* [1968].

3. Experimental Methods

Experiments were conducted in a 180 cm × 15.6 cm × 20.3 cm glass-walled laboratory flume with a horizontal metal bottom (Figure 3). The tank was separated into two reservoirs by a removable 3 ± 0.5 mm thick vertical partition that was positioned at approximately mid-tank. Randomly distributed rigid maple dowels, $d = 0.64$ cm in diameter, were used to model aquatic vegetation which typically has a diameter $d = 10^{-1}$ to 1 cm [e.g., *Leonard and Luther*, 1995]. These dowels were inserted into perforated polypropylene sheets (0.62 holes per cm^2) placed at the bottom of the flume in both reservoirs, directly up to both sides of the partition. The dowels spanned the water column and penetrated the free surface. The range of cylinder densities examined in this paper, $a = 0$ to 0.16 cm^{-1}, produces a dimensionless array density $ad = 0$ to 0.10, which falls within the range observed in natural canopies (e.g., $ad = 0.01$ to 0.1 [*Kadlec*, 1990; *Kalff*, 2002]).

One reservoir was filled with 20 ± 0.2 l of well-mixed saltwater of density ρ_1 and the other with tap water of density ρ_2 ($< \rho_1$) until the free surface in both reservoirs was aligned. For flow visualization, the saltwater was dyed with black or blue food dye in all runs except runs 33 and 34, for which the tap water was dyed instead. The water depth, measured from the top of the perforated base sheets ($z = 0$), was on average $H = 13.6$ cm (Table 1) and varied with the solid volume fraction of the array. This coincides with the low end of typical field depths, which span the range $H = 10$ to 100 cm. In contrast, g' in our study ($g' = 0.5$ to 48.0 cm s^{-2}) was an order of magnitude larger than that typically observed in the field ($g' = 0$ to 1.0 cm s^{-2} [e.g., *Dale and Gillespie*, 1976; *James and Barko*, 1991; *Nepf and Oldham*, 1997]). Consequently, the toe velocity scale $u_{toe} \sim \sqrt{g'H}$ overlaps between field and laboratory conditions.

Experimental runs $1 - 44$ (Table 1) began with the removal of the vertical partition in the middle of the tank. As the two fluids exchanged, a series of 640×480 bitmap images were captured using a Pulnix TM-9701 CCD camera mounted on a stationary tripod in front of the tank. These images were converted to binary images, using a manually selected threshold that appeared, by visual inspection, to most accurately identify the pixels corresponding to the dyed fluid as black. The interface position, $\eta(x, t)$, was located by edge-detection between the white and black pixels. Parallax error is less than 7% and is not corrected for in the analysis. To avoid end effects, only images in the range $H \leq x_{toe} \leq 90 - 1.5H$ were analyzed. The density of the two fluids in all runs except runs 6, 8, 9, 11, and 12 was measured by a hydrometer to ± 0.00025 kg l^{-1}. The densities were also estimated by the mass of salt added, m_{salt}. The fluid temperature was measured to $\pm 1°$C using a thermometer.

To image the entire interface one must forfeit some precision in capturing the evolution of the toe only, i.e., the toe velocity. A second set of experiments (runs A - T) were conducted to more accurately observe the toe velocity. Instead of recording the interface with a CCD camera, a video camcorder followed the leading edge of the undercurrent as it propagated the length of the tank. The times at which the toe passed six or seven pre-selected positions (10 cm $\leq x \leq 71$ cm) were recorded. The densities were estimated from m_{salt} only.

In all fifty-eight experimental runs were conducted; some runs are replicates. The relevant parameters that characterize the flow conditions in each of the experimental runs are summarized in Table 1. Note that data included in the analysis for runs at $ad > 0.01$ were captured after the undercurrent had encompassed a minimum of 5 cylinders (i.e., $x_{toe}B > 5d/a$, where B is the tank width). Therefore, the definition of the array drag in Equation 1 is strictly valid in describing these flows. Flows through sparse arrays, $ad < 0.01$ (runs 8, 9, 11, 26, 28, and 29), and unobstructed flows (runs P - T) remained inertial ($C_D aL/n \leq 2.2$) and the array drag contribution can be considered negligible.

3.1. Processing of Experimental Data

The toe velocity is estimated as the displacement of the toe at the bed between two consecutive images, divided by the difference in time between the two images. The series of images for each run generated a series $u_{toe}(t)$. Because the interface was clearer where dyed fluid was moving into clear water, we only analyze the lower layer. The Re corresponding to u_{toe} is defined as $Re_{toe} = u_{toe}d/\nu$. Then, the array drag at each position, $C_D aL$, is determined using Equation 15 to estimate C_D.

The slope of the interface, $\partial \eta / \partial x$, at $x = 0$ in each image is estimated for runs $1 - 44$ by performing a linear regression on the data points that fall within the range $1.25H - x_{toe} < x < x_{toe} - 1.25H$ for runs with a stem density of $a = 0.068$ cm^{-1}, $a = 0.091$ cm^{-1}, or $a = 0.12$ cm^{-1}, and the range $0 < x < x_{toe} - 1.25H$ for the less densely vegetated runs. The respective ranges were selected to capture as much of the interface as possible without capturing the head of the current at the free surface and the bed. The linear regression was restricted to $x > 0$ for the less densely vegetated runs because of turbulence, which blurs the interface.

The linear drag constant C' was computed from pairs of consecutive images in each experimental run. The two images in the pair are referred to as $i_{previous}$ and $i_{current}$. Because the interface rotates about $\eta = 0.5H$, the velocity near the middle of the interface is very small and the

fractional uncertainty correspondingly large. Because the interface was clearer where dyed fluid was moving into clear water, fitted data were restricted to $\eta < H/3$. Because data points were not necessarily available at the same depths in both images, a polynomial of degree two was fitted to the data points in each image in the range $H/10 < \eta < H/3$ and evaluated at ten evenly spaced depths in the range $0 \leq \eta \leq H/3$. Equation 18 can be rewritten to describe the position of the interface at a given depth,

$$\frac{x_{interface}}{L} = \frac{1}{2} - \frac{z}{H}. \tag{20}$$

Starting from the interface position in $i_{previous}$, the interface in $i_{current}$ was predicted from

$$\frac{dx_{interface}}{dt} = \frac{2\beta}{L} \left(\frac{1}{2} - \frac{z}{H} \right) \tag{21}$$

using 60 time steps in between. The prediction was carried out for a range of C', until a minimum difference, in the least-squared sense, was found between the predicted and observed interface in $i_{current}$. In this manner, a best-fit C' was determined for every pair of images analyzed in a run.

4. Experimental Results

Toe velocities observed in this study ranged from 0.07 to 7.9 cm s^{-1}. These values are similar to those reported in field studies of temperature-driven exchange flows [e.g., *Kalff*, 2002; *MacIntyre et al.*, 2002; *Stefan et al.*, 1989]. The data show that even in the least obstructed scenario (run 11), the viscous stress, which varied between $\nu u_{toe}/(H/2)^2 = 5 \times 10^{-4}$ and 7×10^{-4} cm s^{-2}, was consistently one order of magnitude smaller than the array drag, which ranged from $C_D a u_{toe}^2/2 = 4 \times 10^{-3}$ to 7×10^{-3} cm s^{-2}. This confirms the omission of viscous stress from Equation 1.

The toe velocity of the undercurrent is compared to theory in Figure 4 by normalizing the observed velocity by the classic inertial solution, $\sqrt{g'H/4}$, and by the drag-dominated scale, $\sqrt{\frac{ng'H}{C_D aL}}$ (Equation 13). C_D is estimated from the relation for isolated cylinders (Equation 15), which is appropriate for $ad < 0.03$ [*Nepf*, 1999]. The two theories are compared across a range of array drag, characterized by $C_D aL$. Under low drag conditions, the front propagation is described reasonably well by the classic solution. Overprediction by the classic solution ($\bullet$) at low $C_D aL$ is attributed to turbulence or the neglected bed drag. Indeed, some images indicate shear turbulence near the toe. In contrast, the toe velocity under high drag conditions is better described by the drag-dominated scale ($\circ$). That is, normalization by the drag-dominated scale yields ratios of approximately unity for $C_D aL > 10$, but normalization by the inertial solution yields ratios that decline rapidly as $C_D aL$ increases. As discussed earlier, the flow is expected to become drag-dominated when $C_D aL/n = O(10)$. Since $n \geq 0.92$ in our study, we may simply write this transition point as $C_D aL = O(10)$. This is consistent with Figure 4. Where $C_D aL > 10$, the observed velocity indicates that $u_{toe} = \sqrt{\frac{ng'H}{C_D aL}}$, suggesting that $S_{\eta=0} \approx 0.5$ in Equation 13. This is very close to the slope scale observed at $x = 0$ ($S = 0.6$ for $Re_{toe} > 60$), discussed shortly.

Following from Figure 4, we classify a flow condition as inertial when the observed toe velocity is consistent

with the classic solution (Equation 2). Specifically, we define the dimensionless parameter $\tilde{u}$:

$$\tilde{u} = \frac{observed\ u_{toe}}{\sqrt{\frac{g'H}{4}}}. \tag{22}$$

The presence of drag will suppress $\tilde{u}$ from the classic flow scenario of $\tilde{u} = 1$. For discussion, when $\tilde{u} \geq 0.65$, the flow is classified as inertia-dominated. With this classification, 80% of flows with $C_D aL < 10$ and 97% of flows with $C_D aL > 10$ in Figure 4 are appropriately classified as inertia-dominated and drag-dominated, respectively.

Figure 5 displays the progression of the interface under the three regimes: (a) inertial; (b) non-linear array drag; and (c) linear array drag. Recall that Re dictates the nature of the drag law. First, Figure 5(a) depicts the inertial regime. The interface is horizontal at $\eta \approx 0.5H$. Near the leading edge, the interface bends sharply to the bed ($\eta = 0$) over a longitudinal distance of approximately one water depth. The curved head exhibits good agreement with *Benjamin*'s [1968] solution, shown as a dashed line. Also, there is evidence of turbulent undulations at the interface. These observations are consistent with others reported for the classic, unobstructed lock exchange (see *Simpson*, 1997 for a description).

Next, Figure 5(b) represents a drag-dominated regime in which Re is sufficiently high that a non-linear drag law applies. The general shape of the interface remains similar to the inertia-dominated flow (i.e., it is non-linear), but the interface is now at a slight angle to the bed. The difference from the inertial regime is highlighted by the poor agreement of the experimental data illustrated in (b) with *Benjamin*'s [1968] solution. Also, note that the toe velocity declines as L increases (Equation 13).

Finally, Figure 5(c) represents the linear drag law regime with an essentially linear interface, as described by Equation 18. The head, while still identifiable, is much less prominent than in (a) and (b). Consequently, for the same interface length, the interface gradient at $x = 0$ is greater in magnitude than in (a) and (b) which have lower drag. This trend is similar to that observed for steady gravity currents propagating through screens. As the screen drag increased, the interface gradient at the screen increased [*Rottman et al.*, 1985]. Also, note that the toe advances non-linearly with time, reflecting the decline in u_{toe} as L increases, as predicted by Equation 19. Finally, observe that each interface in Figure 5 rotates approximately about mid-depth, which is consistent with the present theory.

Because all fronts are initiated at $C_D aL = 0$, all flows begin in the inertial regime. A flow may transition from inertial to drag-dominated when $C_D aL$ becomes sufficiently large. This regime transition was captured for $g' = 1.0$ cm s^{-2} and an array of density $a = 0.068$ cm^{-1} (Figure 6). Initially, x_{toe} varies linearly with time ($r^2 = 1.00$, n = 16), as expected in the inertial regime, i.e., u_{toe} is constant in time (Equation 2). At $C_D aL \approx 10$ the toe clearly begins to decelerate and at $C_D aL \approx 20$ it has transitioned to a $\sqrt{t}$ dependence, consistent with the linear drag regime (Equation 19). In this case, the transition begins when the interface spanned half of the tank length.

Next we consider the interface gradient. As illustrated in Figure 1(i) and (ii), respectively, the energy-conserving inertial flow has zero interface slope except near the toe, while the triangular profile in the linear drag regime exhibits a spatially constant interface gradient of $\partial\eta/\partial x = -H/L(t)$. Therefore, the scale constant S

(as defined in Equation 12) at $x = 0$ is $S_0 \equiv S(x = 0) = 0$ and 1 for the inertial and linear drag regime, respectively. The parameter S_0 is computed from the observed interface slope at $x = 0$ as

$$S_0 = \frac{\frac{\partial \eta}{\partial x}|_{x \approx 0}}{-\frac{H}{L}} \qquad (23)$$

for all images with sufficient data points to define the gradient and from which the position of the toe can be extracted.

The behavior of S_0 with changing Re_{toe} is plotted in Figure 7 for all drag-dominated conditions ($C_D a L > 10$). S_0 is nearly constant for $Re_{toe} > 300$ at $S_0 = 0.60 \pm 0.06$ (standard deviation). As stated earlier, a constant S_0 implies a self-similar evolution of the interface profile. S_0 exhibits greater scatter in the range $60 \leq Re_{toe} \leq 300$ at $S_0 = 0.64 \pm 0.08$. Below $Re_{toe} \approx 60$, S_0 progressively increases as Re_{toe} decreases. Note that the perfectly linear interface corresponds to $S_0 = 1$. In the current laboratory study this theoretical maximum was not reached (Figure 7). This is due to the persistence of a slight deviation of the profile at the bed, even when the core region of the interface is linear (Figure 5(c)). Because a small toe persists, the vertical extent of the core region, H^*, is less than H, making the observed interface slope at $x = 0$ smaller than the theoretical slope i.e., $|-H^*/L| < |-H/L|$, and $S_0 (= H^*/H)$ less than 1. This deviation may be a result of Re near the bed not being sufficiently small for C_D to be inversely proportional to Re or the presence of unaccounted momentum sinks, such as the bed drag from the perforated sheets lining the bed. Based on Figure 7, interfaces with $S_0 < 0.75$ and $S_0 \geq 0.75$ are classified as non-linear and linear, respectively. The transition occurs at $Re_{toe} \approx 60$.

It is convenient to classify the exchange flows in a schematic, as shown in Figure 8. Although some overlap exists, the flows are largely segregated in the $C_D a L - Re_{toe}$ plane, and approximate boundaries can be defined at $C_D a L = 7$ and $Re_{toe} = 60$. These threshold values correctly classify all but 17 out of 133 measurements into inertial and non-linear and linear drag regimes (Figure 8). Furthermore, these threshold values are consistent with those predicted from scaling the momentum equation ($C_D a L = O(10)$) and from known transitions in C_D due to cylinder wake behavior, which changes rapidly at the onset of vortex shedding at $Re = O(100)$.

The regime classification presented in Figure 8 can assist in the prediction of toe velocity and flux in the field based on easily measurable parameters. Given a, d, ν, H, and g', we first predict the inertial toe velocity and the corresponding $C_D a L$ at a given L from Equations 2 and 15. If canopy drag is significant ($C_D a L > 7$), we can predict the toe velocity from $u_{toe} = \sqrt{\frac{n g' H}{C_D a L}}$ and Equation 15 iteratively. Then, based on Figure 8 we can anticipate if the vertical profile of the velocity is non-linear or linear. This classification is important in estimating the net flux, because the velocity profile dictates the flux associated with each layer. As an example, predictions are made for a current propagating in a canopy of $d = 0.5$ cm-reeds by applying field temperature measurements by *James and Barko* [1991] in a 1 m-deep littoral zone. Our model predicts that the density gradient associated with a horizontal temperature gradient of $1°C$ per 20 m will drive flow in the linear drag regime even with a canopy density as low as $a = 0.01$ cm^{-1} (Figure 8). In this scenario, the canopy drag decelerates the flow from the unobstructed speed of $u_{toe} = 2.0$ cm s^{-1}

to $u_{toe} = 0.63$ cm s^{-1}. This current would require over 7 hours to propagate 100 m across this littoral region with $a = 0.01$ cm^{-1}. Furthermore, a must be reduced by an order of magnitude before the flow enters the inertial regime. In contrast, a temperature gradient of 1°C per 6 m will have an associated flow in the non-linear drag law regime. This simple exercise suggests the importance of including canopy drag in mathematical models of convective circulation.

Finally, the dimensionless linear drag constant $C'd/\nu$ extracted from flows in the linear profile regime is $C'd/\nu = 310 \pm 90$ (n = 13) for $d = 0.64$ cm. This value may be applied to field estimates instead of Equation 15 when $Re_{toe} < 52$ and for $0.044 < ad < 0.079$, reflecting the range of the conditions considered here.

5. Conclusion

A mathematical description of lock exchange in a random array of rigid emergent cylinders was derived from the conservation of momentum. When $C_D aL < 7$, the gravity current was inertial, regardless of g'. When $C_D aL > 7$, the array drag noticeably decelerated the current. As shown in Figure 6, this transition can occur within the evolution of a single current. Furthermore, linear interfaces were observed in flows where $Re_{toe} < 60$ and $C_D aL > 7$. The present study provides a template for understanding flow regimes that arise from the presence of vegetation and insight into ways in which hydrodynamic effects of rigid vegetation may be incorporated into numerical models of convective circulation [e.g., *Horsch and Stefan*, 1988].

References

Adams, E. E., and S. A. Wells (1984), Field measurements on side arms of Lake Anna, VA, *J. Hydraul. Eng.*, *110*(6), 773–793.

Benjamin, T. B. (1968), Gravity currents and related phenomena, *J. Fluid Mech.*, *31*, 209–248.

Brenner, H., and D. A. Edwards (1993), *Macrotransport Processes*, 1st ed., Butterworth-Heinemann, Stoneham, MA.

Brocard, D. N., and D. R. F. Harleman (1980), Two-layer model for shallow horizontal convective circulation, *J. Fluid Mech.*, *100*, 129–146.

Burke, R. W., and K. D. Stolzenbach (1983), Free surface flow through salt marsh grass, *MIT Sea Grant College Program Report MITSG 83-16*, Massachusetts Institute of Technology, Cambridge.

Coates, M., and J. Ferris (1994), The radiatively driven natural convection beneath a floating plant layer, *Limnol. Oceanogr.*, *39*(5), 1186–1194.

Dale, H. M., and T. Gillespie (1976), The influence of floating vascular plants on the diurnal fluctuations of temperature near the water surface in earliy spring, *Hydrobiologia*, *49*(3), 245–256.

Farrow, D. E., and J. C. Patterson (1993), On the response of a reservoir sidearm to diurnal heating and cooling, *J. Fluid Mech.*, *246*, 143–161.

Horsch, G. M., and H. G. Stefan (1988), Convective circulation in littoral water due to surface cooling, *Limnol. Oceanogr.*, *33*(5), 1068–1083.

Horsch, G. M., H. G. Stefan, and S. Gavali (1994), Numerical simulation of cooling-induced convective currents on a littoral slope, *Intl. J. Num. Meth. Fluids*, *19*(2), 105–134.

Huppert, H. E., and A. W. Woods (1995), Gravity-driven flows in porous layers, *J. Fluid Mech.*, *292*, 55–69.

James, W. F., and J. W. Barko (1991), Estimation of phosphorous exchange between littoral and pelagic zones during nighttime convective circulation, *Limnol. Oceanogr.*, *36*(1), 179–187.

Kadlec, R. H. (1990), Overland flow in wetlands: Vegetation resistance, *J. Hydraul. Eng.*, *116*(5), 691–706.

Kalff, J. (2002), *Limnology : inland water ecosystems*, 1st ed., Prentice-Hall, Upper Saddle River, NJ.

Keulegan, G. H. (1954), Ninth progress report on model laws for density currents. An example of density current flow in permeable media, *National Bureau of Standards Report 3411*, U.S. Department of Commerce, Washington, D.C.

Koch, D. L., and A. J. C. Ladd (1997), Moderate reynolds number flows through periodic and random arrays of aligned cylinders, *J. Fluid Mech.*, *349*, 31–66.

Lei, C., and J. Patterson (2002), Natural convection in a reservoir sidearm subject to solar radiation: experimental observations, *Experiments in Fluids*, *32*(5), 590–599.

Leonard, L. A., and M. E. Luther (1995), Flow hydrodynamics in tidal marsh canopies, *Limnol. Oceanogr.*, *40*(8), 1474–1484.

MacIntyre, S., J. R. Romero, and G. W. Kling (2002), Spatial-temporal variability in surface layer deepening and lateral advection in an embayment of Lake Victoria, East Africa, *Limnol. Oceanogr.*, *47*(3), 656–671.

Monismith, S. G., J. Imberger, and M. L. Morison (1990), Convective motions in the sidearm of a small reservoir, *Limnol. Oceanogr.*, *35*(8), 1676–1702.

Nepf, H. M. (1999), Drag, turbulence, and diffusion in flow through emergent vegetation, *Water Resour. Res.*, *35*(2), 479–489.

Nepf, H. M., and C. E. Oldham (1997), Exchange dynamics of a shallow contaminated wetland, *Aquat. Sci.*, *59*(3), 193–213.

O'Donnell, J. (1993), Surface fronts in estuaries: A review, *Estuaries*, *16*(1), 12–39.

Oldham, C. E., and J. J. Sturman (2001), The effect of emergent vegetation on convective flushing in shallow wetlands: Scaling and experiments, *Limnol. Oceanogr.*, *46*(6), 1486–1493.

Raupach, M. (1992), Drag and drag partition on rough surfaces, *Boundary-Layer Meteorol.*, *60*, 375–395.

Roget, E., and J. Colomer (1996), Flow characteristics of a gravity current induced by differential cooling in a small lake, *Aquat. Sci.*, *58*(4), 367–377.

Roget, E., J. Colomer, X. Casamitjana, and J. E. Llebot (1993), Bottom currents induced by baroclinic forcing in Lake Banyoles (Spain), *Aquat. Sci.*, *55*(3), 206–227.

Rottman, J. W., J. E. Simpson, J. C. R. Hunt, and R. E. Britter (1985), Unsteady gravity current flows over obstacles: Some observations and analysis related to the phase II trials, *J. Hazard. Mater.*, *11*, 325–340.

Shin, J. O., S. B. Dalziel, and P. F. Linden (2004), Gravity currents produced by lock exchange, *J. Fluid Mech.*, *521*, 1–34, doi:10.1017/S002211200400165X.

Simpson, J. E. (1997), *Gravity currents in the environment and the laboratory*, 2nd ed., Cambridge University Press, New York.

Stefan, H. G., G. M. Horsch, and J. W. Barko (1989), A model for the estimation of convective exchange in the littoral region of a shallow lake during cooling, *Hydrobiologia*, *174*(3), 225–234.

Sturman, J. J., and G. N. Ivey (1998), Unsteady convective exchange flows in cavities, *J. Fluid Mech.*, *368*, 127–153.

Wells, M. G., and B. Sherman (2001), Stratification produced by surface cooling in lakes with significant shallow regions, *Limnol. Oceanogr.*, *46*(7), 1747–1759.

White, F. M. (1991), *Viscous Fluid Flow*, 2nd ed., McGraw-Hill, New York.

Y. Tanino and H. M. Nepf, Department of Civil and Environmental Engineering, Massachusetts Institute of Technology, 77 Massachusetts Avenue 48-216, Cambridge, MA 02139, USA. (ytanino@mit.edu; hmnepf@mit.edu)

P. S. Kulis, Department of Civil Engineering, University of Texas at Austin, Pickle Research Campus Bldg 119, MC R8000, Austin, TX 78712, USA. (paulakulis@mail.utexas.edu)
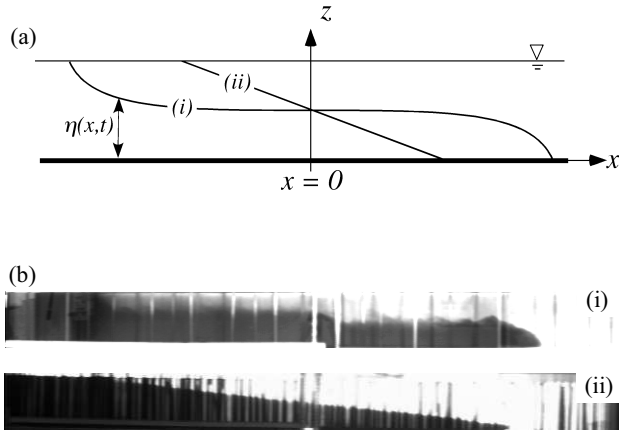
(a)

(b)

Figure 1. Comparison of the interface profile, $\eta(x,t)$, in the (i) inertia- and (ii) drag-dominated regimes. $\eta(x,t)$ is the vertical distance from the bed to the interface. At $x = 0$ the gradient of the interface, $\partial\eta/\partial x$, is zero for inertia-dominated regimes and $\partial\eta/\partial x < 0$ for drag-dominated regimes. Note that the white bar at the bottom of (b)(i) is a ruler taped on the tank wall, and not the bed.
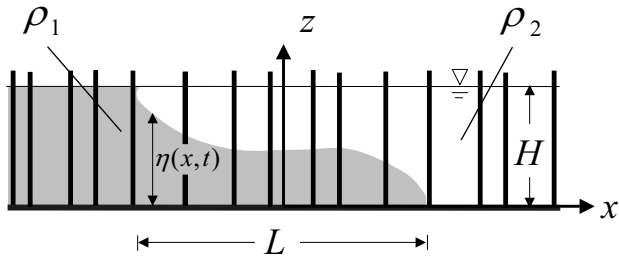

Figure 2. Schematic of a lock exchange within a cylinder array. Lock positioned at $x = 0$. H is water depth; L is the longitudinal length of the interface; and ρ_1 and ρ_2 are the density of the denser (grey) and lighter (white) fluid, respectively.
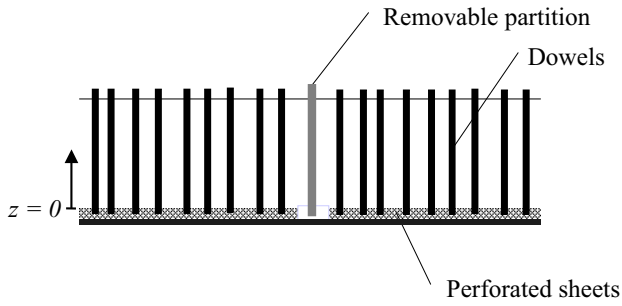
Figure 3. Side view of the central section of the labora-tory tank and the random array of emergent cylindrical dowels. Dowels were inserted in perforated sheets placed at the bottom of the tank. The interface between the fluid and the perforated sheets is defined as $z = 0$. The length of the tank is $L_{tank} = 180$ cm.
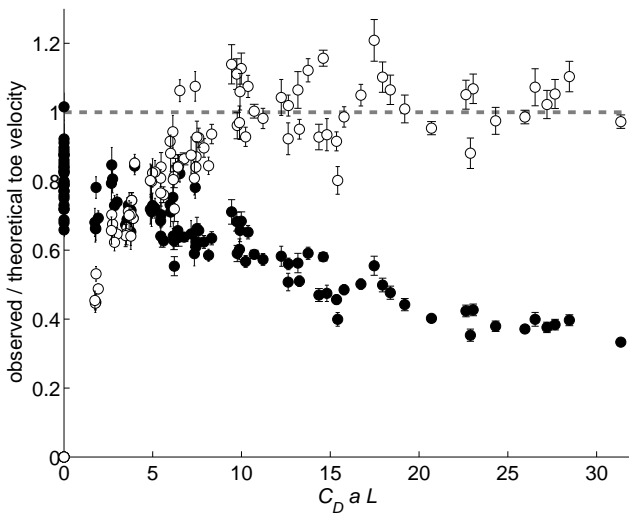

Figure 4. Ratio of observed and theoretical toe ve-locities for runs A - T using the inertial theory (Equa-tion 2) $\sqrt{\frac{g'H}{4}}$ (●) and the drag-dominated velocity scale $\sqrt{\frac{ng'H}{C_D aL}}$ (○), with C_D for isolated cylinders (Equation 15; Re is based on the measured toe velocity). The drag-dominated theory is consistent with the observed velocity at high $C_D aL$, but rapidly deviates from the observations as $C_D aL \to 0$. (Note data at $C_D aL = 0$.) In contrast, the inertial theory describes the observation well at low $C_D aL$, but deviates rapidly for $C_D aL > 5$. The vertical bars represent uncertainty in the observed toe velocities.
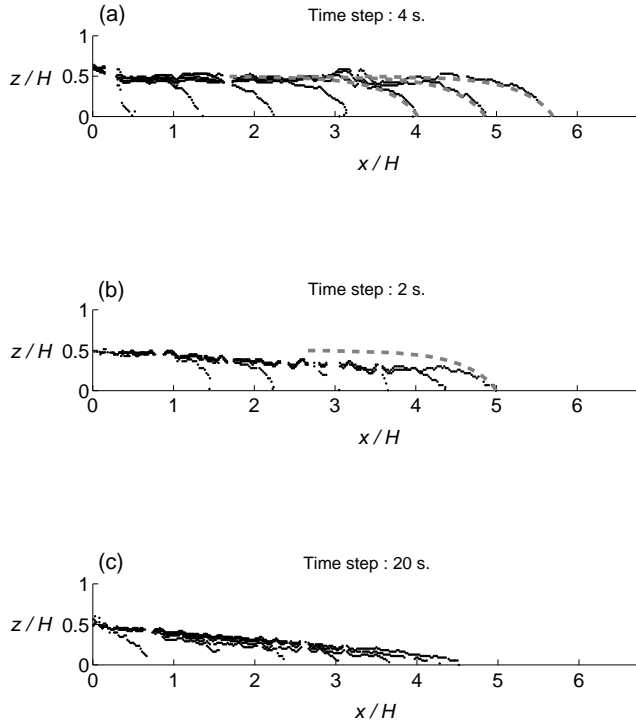
Figure 5. Progression of the interface with time. The profiles are separated by the time step indicated at the top of each subplot. The horizontal axes span $0 \leq x \leq L_{tank}/2$. (a) Run 9: $Re = 190 - 200$ and $C_D aL = 0.88 - 1.9$; (b) Run 42: $Re = 190 - 260$ and $C_D aL = 6.9 - 12$; (c) Run 31: $Re = 8.4 - 53$ and $C_D aL = 11 - 27$. Dashed curves represent *Benjamin* [1968]'s solution for energy-conserving gravity currents.
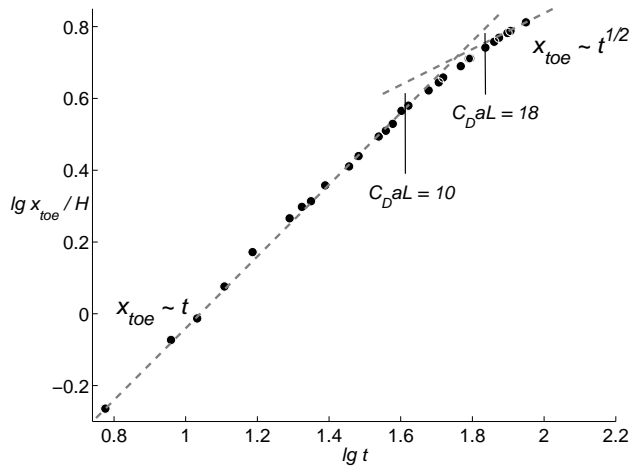

Figure 6. Temporal evolution of the toe position. The dashed lines illustrate the time-dependence predicted by Equation 2 for inertial conditions (i.e., $x_{toe} \sim t$) and consistent with Equation 18 for linear drag conditions (i.e., $x_{toe} \sim \sqrt{t}$).
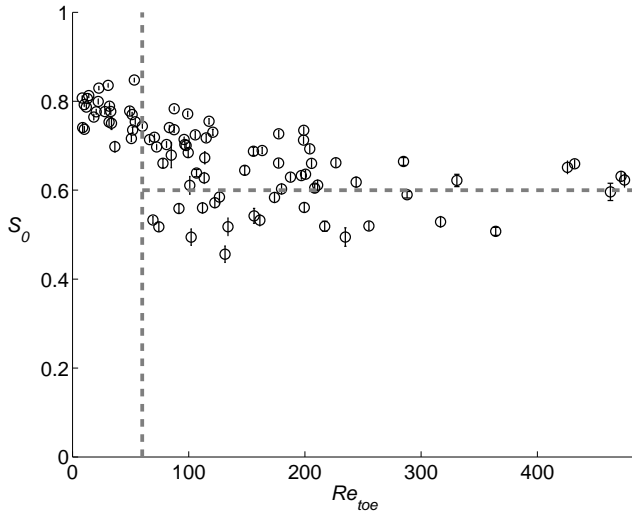
Figure 7. Slope scale S estimated at $x = 0$ (Equation 23) under drag-dominated conditions. A regime transition occurs at $Re_{toe} = 60$. Vertical bars indicate the maximum uncertainty in the gradient of the linear regression performed on the interface.
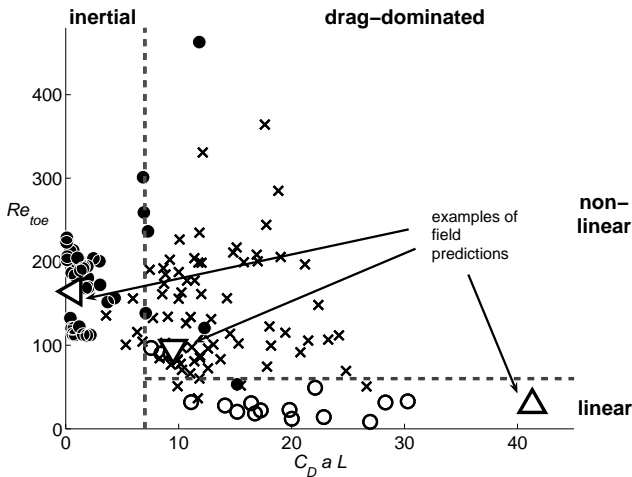

Figure 8. Segregation of exchange flows into three regimes by empirical boundaries $Re_{toe} = 60$ and $C_D aL = 7$. These criteria consistently segregate flows with corresponding $\tilde{u} \geq 0.65$ (●), $\tilde{u} < 0.65$ and $S_0 \geq 0.75$ (○), and $\tilde{u} < 0.65$ and $S_0 < 0.75$ (×) into their correct regimes. Field conditions from (i) *James and Barko* [1991] and (ii) *Dale and Gillespie* [1976] are applied in a hypothetical canopy of reeds ($a = 0.01$ cm^{-1}; $d = 0.5$ cm) with (i) $H = 100$ cm (temperature of the two fluids are $T_1 = 16°$C and $T_2 = 17°$C and $L = 20$ m ($\triangle$); $T_1 = 26°$C and $T_2 = 27°$C and $L = 6$ m ($\triangledown$)); and (ii) $H = 50$ cm at $T_1 = 14.0°$C and $T_2 = 20.0°$C and $L = 50$ cm ($\triangleleft$). C_D is estimated by Equation 15.

Table 1. Summary of Experimental Conditions and Model Parameters.

Run Number	Frontal Area Per Unit Volume, a	Mass of Salt Added, m_{salt}	Reduced Gravity, g'^{a}	Mean Water Depth, H
	$\pm$ **0.5%** [stems/cm]	$\pm$ **0.05 g** [g]	$\pm$ **0.3 cm s^{-2}** [cm/s^2]	$\pm$ **0.6 cm** [cm]
1	0.12	1393.80	43.2	14.0
2	0.12	1468.77	48.0	14.2
3	0.12	500.00	18.9	13.5
4	0.091	100.00	3.8	13.5
5	0.068	100.00	4.0	13.7
6	0.023	100.00	3.9	13.3
7	0.12	100.00	3.9	13.9
8	0.0046	100.00	3.9	13.2
9	0.011	100.00	3.9	13.3
11	0.00091	100.00	3.9	13.5
12	0.12	10.00	1.2	13.9
13	0.091	100.00	3.9	13.7
14	0.12	502.43	18.7	13.7
16	0.12	700.00	24.1	14.3
17	0.12	1000.00	33.8	13.8
18	0.12	500.00	18.7	13.9
19	0.12	750.00	26.2	14.0
20	0.12	100.00	4.0	14.0
21	0.046	100.00	3.9	13.0
23	0.091	100.00	4.2	13.4
26	0.011	190.00	7.1	12.8
27	0.023	190.00	6.5	12.9
28	0.0046	100.00	4.1	12.8
29	0.011	100.00	4.4	13.0
30	0.068	10.00	0.6	13.6
31	0.068	10.00	0.5	13.4
32	0.068	10.00	0.5	13.4
33	0.068	50.00	2.2	13.4
34	0.068	50.00	2.1	13.5
35	0.068	50.00	1.9	13.3
36	0.068	100.00	4.0	13.5
37	0.068	100.00	4.0	13.4
38	0.068	100.00	4.0	13.3
39	0.068	300.00	13.2	13.1
40	0.068	300.00	13.2	13.4
42	0.068	500.00	18.1	13.3
43	0.068	500.00	18.1	13.4
44	0.068	500.00	18.1	13.3
A	0.16	126.81	5.0	14.0
B	0.16	252.14	9.2	14.3
C	0.16	380.71	14.0	14.1
D	0.16	504.07	17.8	14.3
E	0.16	630.14	22.1	14.3
F	0.091	126.00	4.4	13.8
G	0.091	252.00	9.2	13.8
H	0.091	402.30	14.7	13.9
I	0.091	504.00	18.0	14.0
J	0.091	631.00	22.7	14.0
K	0.046	127.00	4.3	13.8
L	0.046	254.19	9.1	13.2
M	0.046	379.71	13.6	13.5
N	0.046	504.44	17.8	13.2
O	0.046	626.45	21.8	13.7
P	0	127.71	4.1	14.0
Q	0	250.70	8.9	14.0
R	0	375.55	13.2	13.3
S	0	513.86	18.3	13.1
T	0	675.80	23.6	14.0

$^{\text{a}}$ The g' values presented here for runs 1 - 44 have been corrected for temperature, and the density values used to calculate them were slightly different from the uncorrected measurements.